WILEY | The International Journal of **Medical Robotics** and **Computer Assisted Surgery**

ORIGINAL ARTICLE

Intraocular robotic interventional surgical system (IRISS): Mechanical design, evaluation, and master–slave manipulation

Jason T. Wilson[1] | Matthew J. Gerber[1] | Stephen W. Prince[1] | Cheng-Wei Chen[1] | Steven D. Schwartz[2] | Jean-Pierre Hubschman[2] | Tsu-Chin Tsao[1]

[1]Department of Mechanical and Aerospace Engineering, Los Angeles, CA, UCLA, USA
[2]Jules Stein Eye Institute, Los Angeles, CA, UCLA, USA

Correspondence
Tsu-Chin Tsao, Department of Mechanical and Aerospace Engineering, UCLA, Los Angeles, CA, USA.
Email: ttsao@ucla.edu

Abstract

Background: Since the advent of robotic-assisted surgery, the value of using robotic systems to assist in surgical procedures has been repeatedly demonstrated. However, existing technologies are unable to perform complete, multi-step procedures from start to finish. Many intraocular surgical steps continue to be manually performed.

Methods: An intraocular robotic interventional surgical system (IRISS) capable of performing various intraocular surgical procedures was designed, fabricated, and evaluated. Methods were developed to evaluate the performance of the remote centers of motion (RCMs) using a stereo-camera setup and to assess the accuracy and precision of positioning the tool tip using an optical coherence tomography (OCT) system.

Results: The IRISS can simultaneously manipulate multiple surgical instruments, change between mounted tools using an onboard tool-change mechanism, and visualize the otherwise invisible RCMs to facilitate alignment of the RCM to the surgical incision. The accuracy of positioning the tool tip was measured to be 0.205 ± 0.003 mm. The IRISS was evaluated by trained surgeons in a remote surgical theatre using post-mortem pig eyes and shown to be effective in completing many key steps in a variety of intraocular surgical procedures as well as being capable of performing an entire cataract extraction from start to finish.

Conclusions: The IRISS represents a necessary step towards fully automated intraocular surgery and demonstrated accurate and precise master-slave manipulation for cataract removal and—through visual feedback—retinal vein cannulation.

KEYWORDS
calibration, computer assisted surgery, image analysis, kinematics, mechatronics, robot design

1 | INTRODUCTION

Ever since the advent of robot-assisted surgery in 1985, the value of using robotic systems to assist in surgical procedures in the modern operating theatre has been demonstrated repeatedly.[1] However, most intraocular surgical procedures continue to be performed manually by surgeons. One of the most common procedures is cataract surgery, which is performed approximately 2.5 million times a year in the United States alone.[2] With the use of femtosecond lasers, emerging technologies have enabled autonomous completion of specific steps of cataract surgery, including capsulorhexis and lens fragmentation.[3–5] While effective in performing such procedures, laser-based technologies are unable to perform surgical steps that require physical manipulation, such as removal of an emulsified lens or insertion of an intraocular lens implant. In addition to intricate physical manipulation,

a complete cataract surgery can require simultaneous manipulation of two surgical instruments, a range of motion up to 180° about each major rotational axis,[6] two remote centres of motion (RCMs) in close proximity, and an array of surgical instruments— at least one of which is uniquely associated with each surgical step.[7]

The majority of research on intraocular surgical robotics has been directed towards both anterior segment surgery and vitreoretinal surgery. Feline retinal vessel cannulation was achieved by Grace[8] using a micropipette mounted to a modified parallel manipulator invented by Merlet.[9] Similar to Bourla,[10] Bourges[11] evaluated the feasibility of using the da Vinci Surgical System (Intuitive Surgical, Inc.) to position a parallel micromanipulator at the surgical insertion point in the eye. It was found that the range of motion was too small to perform manoeuvers in both the posterior and anterior sections of the eye. A solution to this lack of dexterity was proposed by Wei[12,13] through the addition

wileyonlinelibrary.com/journal/rcs

of extra degrees of freedom to the surgical instrument inside the eye, which is inconsistent with currently accepted intraocular practice. Nasseri[14-16] applied a parallel-coupled joint mechanism to achieve an adjustable pivot point. Vitreo-retinal surgery was realized by implementing force feedback as a user interface while removing tremors caused by human motions.[17] The University of Tokyo[18-20] developed an integrated robotic surgical system composed of a master manipulator, spherical prismatic slave manipulator and a high-definition visualization system. With this system, the authors performed posterior vitreous detachment, retinal vessel sheathotomy and microcannulation. Serving as a retinal vessel phantom, the vessels in the chorioallantoic membrane of a chicken embryo were successfully cannulated by Mitchel[21] using a cooperative instrument manipulator.[22]

The aforementioned robotic devices all employed a single mounted instrument. In contrast, the work He[23] and Smet de[24] realized a two-manipulator slave robot with a tool-change mechanism. The design of the onboard tool-change mechanism supported five different instruments on each manipulator arm. However, due to the mechanical complexity of the proposed design, only a single-tool version was implemented. In addition, the parallelogram-based mechanism limits the range of motion to 90° along the major rotational axes, and alignment of the RCM to the eye is tedious because the RCM is invisible. Such issues must be addressed before the robotic platform can be applied to clinical trials.

A novel robotic system — the IRISS— aimed at remotely operated and fully automated intraocular mechanical manipulations has been developed. Compared to the work presented by He[23] and Smet de[24] the IRISS features a simpler tool-change mechanism, a set of low-power lasers to align the RCM to the surgical incision in the eye, and a larger range of motion that covers the entire hemisphere and allows simultaneous manipulation of two tools on two arms in close proximity without interference. Initially, the IRISS was used to perform cataract extraction, and its evaluation on animal models has been reported in reported by Rahimy[25]. The current paper highlights the details of the mechanical design and the mechanical evaluation of the IRISS. The paper is organized as follows: section 2 introduces the clinical requirements for intraocular surgery; section 3 describes the mechanical design of the IRISS; section 4 discusses the hardware–software interface and the method of control; section 5 evaluates the performance of the robot, both mechanically and in a clinical trial; and section 6 concludes the paper.

2 | REQUIREMENTS FOR EYE SURGERY

The design of the IRISS is motivated by the goal of performing complete, multistep intraocular surgical procedures to successful completion. Many such procedures require the ability to use two instruments simultaneously inside the eye and the ability to change between surgical tools during surgery. For procedures that do not require the simultaneous use of two tools, the ability to safely transition between tools during a multistep process can reduce total operational time. Common tools for both anterior and posterior segment surgery include a viscoelastic syringe, an irrigating needle, an infusion–aspiration probe, a light pipe, a vitreous cutter and a cannula. Depending on the type of surgery, not all of these tools are required. The use of many other tools is possible,

and it is a requirement to be able to mount any commercially available and commonly employed tool.

At least two methods exists for reducing stress at the entry site during surgery: (1) using active software enforcement with visual or force-based feedback control to minimize tool-induced stress and (2) physically constraining the surgical instrument about its incision point in the eye. The first method introduces complexity into the sensors and control software, while the second relies on a mechanically constrained 'pivot point' in the design of the robotic platform. In the second case, the pivot point of the surgical tool must be coincident with the surgical incision for the duration of the surgery. If this condition is not satisfied, then the self-sealing properties of the surrounding corneal tissue may be diminished, resulting in perioperative leakage from the corneal incision or other complications. This clinical requirement suggests the use of a mechanically constrained RCM and forms the basis for the mechanical design of the IRISS.

The RCM must be capable of three-dimensional translation with respect to the patient (up to 25 mm along each axis). This is for two reasons: to align the mechanical RCM of the robot to the surgical incision in the cornea (to reduce stress at the entry site) and to compensate for eyeball movement during surgery. The second is required because the patient remains conscious during many procedures, and eye movement may not be entirely fixed.

In addition, the robot must possess a sufficiently large workspace to position and orientate the surgical instrument inside the eye to successfully perform desired procedures. A typical human eyeball has transverse and sagittal diameters of approximately 24 mm.[7] Three degrees of freedom are required for three-dimensional positioning of the tool tip inside the eyeball, while a fourth is necessary for axial rotation of the tool. The fourth degree of freedom is especially important in lens aspiration, where the surgical tool is rotated for aspiration and irrigation of the lens. Also, the workspace of the manipulator must not interfere with—and must fit under—a standard surgical microscope (average focal distance of 185–235 mm). In summary, the clinical design requirements of the IRISS are to:

1. simultaneously employ two instruments inside the eye;
2. readily change between mounted tools during surgery;
3. constrain the active tools about RCMs;
4. translate the RCMs by 25 mm in all three dimensions;
5. possess a sufficiently large workspace to encompass the entire eyeball;
6. exhibit four degrees of freedom for the tool tip;
7. fit under a standard surgical microscope.

3 | MECHANICAL DESIGN

The IRISS is designed for both master–slave and automated manipulations. The slave manipulator includes two independently controllable arms, each holding two automatically interchangeable surgical instruments, which are both mounted to a carriage riding on a circular track (Figure 1). This configuration was designed to (1) provide minimal interference with a surgical camera and microscope, (2) allow a 50th percentile male head to be contained within the workspace without collision, and (3) allow intuitive mapping between the master surgical controller and the IRISS. The surgical instruments are mechanically
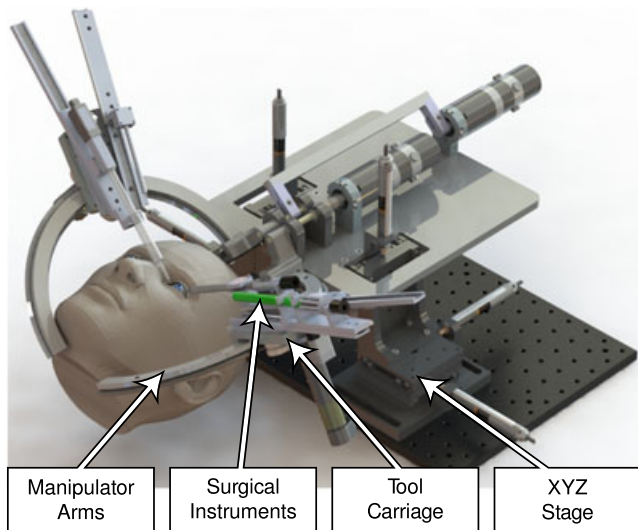
FIGURE 1 Computer-aided design (CAD) model of the IRISS slave manipulator (isometric view)

constrained about an RCM with each being independent of the other. Many types of commercially available microsurgical instruments have been adapted to fit onto the surgical manipulator. The robotic motion is actuated by brushed DC motors and driven by current-type drive electronics.

To meet the design requirements, the IRISS is capable of concurrently mounting four tools and switching between them during surgery. The tools operate independently from each other, but both arms possess RCMs that are simultaneously enforced and in close proximity to each other (10–12 mm). This setup allows for one arm to manipulate the eyeball pose while the other engages in an operation—similar to how a human surgeon manipulates an eyeball to facilitate position and access. The four required degrees of freedom (per tool) are labeled as θ_1 and θ_2: rotation about two orthogonal axes which intersect at the RCM, d_3: translation in and out of an eye along the tool centreline, and θ_4: rotation about the tool centreline. In addition, each tool possesses the ability to translate the position of its RCM relative to the patient for the purpose of aligning to the surgical incision point.

3.1 | Manipulator design

A single manipulator arm is shown with a single tool in Figure 2. The RCM is mechanically enforced by mounting the surgical instruments to a carriage that rides along a circular track (HepcoMotion 180° double-edge ring slide), enabling rotation about $\hat{Y}$ by θ_2. The circular track with its carriage (the manipulator 'arm') is mounted to a rotational joint, which rotates about $\hat{Z}$ by θ_1. These two elements are aligned (see section 3.4) such that their rotational axes are orthogonal and intersect at the RCM. The tool carriage is mounted to the circular track through three v-groove bearings (HepcoMotion PRT2). One bearing has its axis of rotation mounted on a cam, which ensures that the three-point-wheel system is constrained perpendicular to the track's v-groove. The carriage is actuated by a brushed DC motor (Maxon Motor A-max 22; GP 22-A planetary gearhead; MR Type M encoder) attached to one of the outer-diameter bearings. The surgical instruments are mounted such that their centrelines pass through the RCM. The in-and-out translational motion of the tool is defined as d_3 and the tool rotation about its centreline is denoted as θ_4.
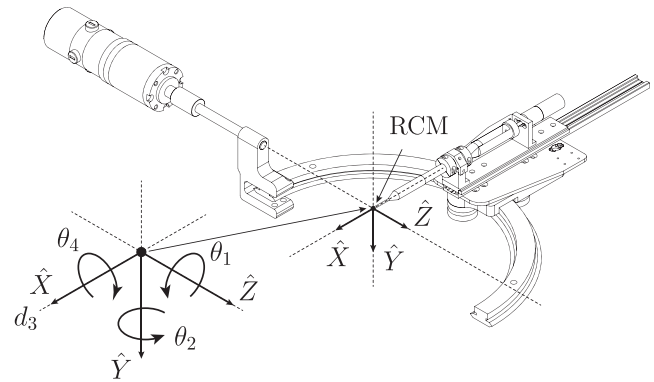

FIGURE 2 Schematic diagram of a single manipulator arm with definitions of the coordinate frame and kinematic variables indicated. All joint axes of rotation and translation are defined coincident with the RCM. The manipulator orientation is shown for $\theta_1 = \theta_2 = \theta_4 = 0$ and $d_3 = 0$

The manipulator arm is mounted to a rotational shaft that is cantilevered off a mounting stage through a series of bearing blocks. The shaft's axis of rotation, $\hat{Z}$, is parallel to the plane of the circular track. The surgical instruments are offset from the carriage in the $\hat{Y}$ direction such that their axes of translation and rotation pass through the axis of the rotational shaft, $\hat{Z}$. As the circular track and tool carriage are rotated about $\hat{Z}$ by the rotational shaft, the intersection point of all axes of motion remains a fixed, stationary point relative to the robotic base frame. This mechanically fixed point is the RCM.

The two identical, mirror-image manipulator arms are mounted to rotational shafts positioned next to each other such that the rotational axes are parallel. The diameter of the shaft and the geometry of the bearing blocks are chosen such that the distance from the shaft centreline to the edge of the bearing block is 7.5 mm. This allows the mechanically constrained, independent RCMs of each arm to be 15 mm apart when the bearing blocks are in contact. Both bearing blocks contain two sealed, needle-roller bearings that provide increased load capacity and allow the bearing blocks to be in close proximity. The rear motor is staggered behind the front motor, with the front motor transmitting torque to the mechanism arm in a direct-drive manner (see Figure 1). A crank shaft is used to transmit torque from the rear motor to its arm. To reduce backlash and improve accuracy of the IRISS, both front and rear motors were chosen to be Harmonic Drive 'zero backlash' RH-11D-3001 DC motors with E100 encoders.

Tool exchange and translational motion of a surgical instrument along its centreline axis are achieved by the same mechanism, as shown in Figure 3. Each surgical instrument—regardless of type—is mounted on a linear slide (Igus drylin NK-02-17). The slides are offset by an angular distance of $\phi_f = 0.175$ rad to prevent physical interference. The d_3 translational motion is actuated by a brushed DC motor (Maxon Motor RE 13; GP-13-A planetary gearhead; MR Type-S encoder). The sliding mechanism has a full translational range of 85 mm: 25 mm beyond the RCM point ('into' the eyeball) and 60 mm in the retracted direction ('away' from the eyeball). This range is large enough that a fully retracted surgical instrument does not physically interfere with the tool mounted beside it or with the patient's head. The output torque of the d_3 motor is converted to linear force via a nylon rack-and-pinion mechanism secured to the side of the slider. The initial d_3 position of
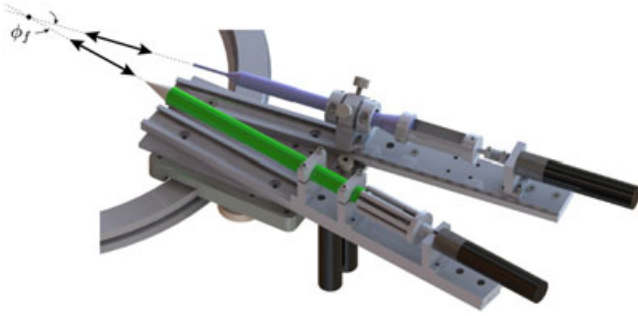
FIGURE 3 CAD model of the mechanism that facilitates d_3 translation and changing between mounted surgical instruments

the slider is calibrated with use of a photo-interrupter sensor (Honeywell HOA7720), which is used to provide a reliable 'zero' position for the d_3 translation. The θ_4 rotational motion is actuated by a brushed DC motor (Maxon Motor RE 13; GP-13-A planetary gearhead; MR Type-S encoder) with a rotational range of ±0.52 rad. The initial θ_4 angle is also calibrated with a photo-interrupter sensor (Honeywell HOA7720), which is used to provide a reliable angular 'homed' position.

To allow three-dimensional translation of the mechanically constrained RCM, both arm assemblies are mounted to stages capable of three-dimensional *XYZ* translation. The stages are composed of three roller guide stages (Saruga Seiki B11-80A, ±12.5 mm travel distance) coupled together with a mounting bracket (Saruga Seiki A47-6) to allow for *Z*-axis travel. The translational motion of the stage is actuated by three DC servo actuators (ThorLabs Z812). An advantageous feature of this configuration is the mechanical decoupling between robotic motions about the RCM (namely, $\theta_1, \theta_2, d_3, \theta_4$) and the *XYZ* translational motion of the RCM with respect to the robotic base frame. An additional benefit includes the possibility of maintaining the alignment of the RCM to the surgical incision point during surgery via tracking of the eyeball movement, though this functionality has not been implemented in the current prototype.

To date, several commercially available microsurgical instruments have been adapted to fit on the surgical manipulator. These include a viscoelastic syringe (Healon; Abbott Medical Optics), a capsulotomy-irrigating needle (modified 30-gauge needle, B-D 30G 1/2, 305128; Becton, Dickinson & Co.), an infusion-aspiration (I/A) probe (Alcon), a 23-gauge light pipe, a 23-gauge vitreous cutter and a 23/36-gauge cannula (Alcon). Aside from the I/A probe, which was dedicated for research and animal study, all other surgical instruments were disposable. The instruments were chosen to form a representational set of common tools and to represent a wide array of physical sizes and dimensions.

3.2 | Master surgical controller

A custom surgical controller was designed as a master input device and is shown in Figure 4. The surgeon holds and manipulates the shaft of the surgical controller as if it were a standard intraocular surgical instrument. Rotation about the axis of the input shaft is measured by an optical encoder and is mapped to rotation of the surgical instrument, θ_4. Translational motion along the input shaft's centreline axis is also measured by an optical encoder, driven by a nylon rack-and-pinion mechanism and mapped to the surgical instrument motion, d_3. This assembly is mounted to a gimbal mechanism with two degrees of freedom with
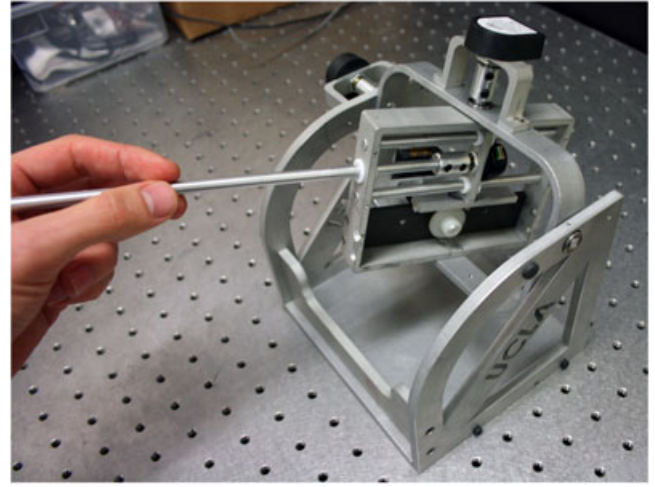

FIGURE 4 Image of the IRISS surgical controller

optical encoders attached to both rotational axes. One rotational axis is mapped to the carriage location along the circular track, θ_2, while the other is mapped to the angular position of the rotational shaft, θ_1. All four encoders are US Digital two-channel S1 optical shaft encoders and the mapping is implemented as one-to-one for the ease of use of the surgeon.

3.3 | Manipulator kinematics

An ideal minimally invasive surgical robotic manipulator has at least three degrees of freedom with all three joint axes intersecting at a single point to create the RCM. To establish the RCM, the IRISS possesses two rotational degrees of freedom (θ_1 and θ_2) and one translational degree of freedom (d_3). The θ_4 rotation about the centreline of the surgical instrument does not affect the RCM in the ideal case, and is therefore ignored in the following analysis. Using the product of exponentials,[26] the ideal forward kinematic map $g_{st}(\theta)$ of the IRISS can be written as

$$g_{st}(\theta) = \left[\begin{array}{ccc|c} c_2 & 0 & s_2 & s_2 d_3 \\ s_1 s_2 & c_1 & -s_1 c_2 & -s_1 c_2 d_3 \\ -c_1 s_2 & s_1 & c_1 c_2 & c_1 c_2 d_3 \\ \hline 0 & 0 & 0 & 1 \end{array}\right] \tag{1}$$

$$= \left[\begin{array}{c|c} R_{st}(\theta) & t_{st}(\theta) \\ \hline 0 & 1 \end{array}\right] \tag{2}$$

where $c_i := \cos(\theta_i)$, $s_i := \sin(\theta_i)$ and joint angles are defined as in Figure 2.

Given a desired point $\boldsymbol{p}^* := [p_x \ p_y \ p_z]^\mathsf{T}$ in the workspace of the manipulator, the inverse kinematics are given by

$$d_3 = \sqrt{p_x^2 + p_y^2 + p_z^2} \tag{3}$$

$$\theta_2 = \text{Atan2}(s_2, c_2), \quad s_2 = \frac{\sqrt{p_x^2 + p_y^2}}{d_3}, \quad c_2 = \frac{-p_z}{d_3} \tag{4}$$

$$\theta_1 = \text{Atan2}(s_1, c_1), \quad s_1 = \frac{p_y}{s_2 d_3}, \quad c_1 = \frac{p_x}{s_2 d_3} \tag{5}$$

where Atan2 is the arctangent function with two arguments.

Although the custom components of the IRISS were fabricated using high-accuracy and repeatable CNC machines, potential sources

of misalignment exist due to error in assembly tolerance stack-up. A comprehensive study of the assembly contacts found a total of 43 points of assembly for a single arm and with consideration of only a single mounted tool. However, 16 points of contact are associated with $\hat{Z}$ and determine the pose of this axis relative to the fixed base. Because all other coordinate frames are defined relative to the $\hat{Z}$ axis, these points of contact can be ignored. Of the remaining 27 points of contact, two significant sources of alignment error arise.

One source of assembly error arises from the fact that the circular track (which determines the pose of $\hat{Y}$) is mounted to the rotational shaft in a way that allows for variation in the translational distance between $\hat{Y}$ and $\hat{Z}$. This variation can result in a translational misalignment of the $\hat{Y}$ axis in the $\hat{X}$ direction, termed ε_x. Misalignments in both the $\hat{Z}$ and $\hat{X}$ directions can be ignored because variation in either direction simply translates the RCM location relative to the fixed robot base but does not eliminate its existence. Rotational variations about the $\hat{Z}$ and $\hat{Y}$ axes can be ignored because angular displacements about these axes are equivalent to the motions θ_1 and θ_2, respectively. Variation about the $\hat{X}$ axis is possible, but was considered negligible because the mount that couples the circular track to the rotational shaft was fabricated in a single CNC operation. This single setup ensured perpendicularity between the through hole for the shaft and the mounting holes for the arc. As a result, the plane of the circular track and the $\hat{X}$ axis should be parallel with little error, even if this distance is not well known.

A second source of assembly error arises from the components between the tool carriage and the surgical instrument itself. These components are the d_3 and θ_4 joints and contain approximately 20 points of contact, depending on the mounted tool type. Specifically, these components consist of the carriage of the circular arc, a linear track and its slider carriages, a tool-mounting plate and an array of components for mounting a surgical instrument. Any assembly or manufacturing error in the height of these components or in the diameter of the surgical-instrument mounts will result in a translational misalignment in the $\hat{Y}$ direction, termed ε_y. In addition, any error in the diameter of the surgical-instrument mounts, or slack between the linear track and its slider carriages, will result in a translational misalignment in the $\hat{Z}$ direction, termed ε_z. On the other hand, each of the possible rotational misalignments corresponds to a desired degree of freedom and can be ignored: angular misalignment about $\hat{Z}$ corresponds to θ_1, $\hat{Y}$ to θ_2, and $\hat{X}$ to θ_4.

By accounting for these three sources of misalignment (ε_x, ε_y, and ε_z), the forward kinematics of the IRISS are now given by

$$\tilde{g}_{st}(\theta) = \left[\begin{array}{c|c} R_{st}(\theta) & \tilde{t}_{st}(\theta) \\ \hline 0 & 1 \end{array} \right] \qquad (6)$$

where $R_{st}(\theta)$ is as before and $\tilde{t}_{st}(\theta)$ is given by

$$\tilde{t}_{st}(\theta) := \left[\begin{array}{c} s_2 d_3 + c_2 \varepsilon_z \\ -s_1 c_2 d_3 + c_1 \varepsilon_y + s_1 s_2 \varepsilon_z - s_1 \varepsilon_x \\ c_1 c_2 d_3 + s_1 \varepsilon_y - c_1 s_2 \varepsilon_z + c_1 \varepsilon_x \end{array} \right].$$

Note that the three sources of error influence the position of the RCM and likewise the tip of the surgical instrument, but *not* the orientation of the instrument relative to the fixed robotic base frame.

Finally, the dynamic effects for this level of precise motion control can be ignored for the master–slave manipulation with the appropriately tuned feed-forward tremor filtering and joint angle feedback control loop. There is a vibration mode for the arm at approximately 13 Hz that challenges the control design, but because the robot is commanded to move at fairly low joint angle velocities (for safety purposes and based on surgeon feedback), the vibration mode was never triggered during typical operation. Similarly, inertial effects, joint acceleration and so on can also be ignored.

3.4 | Mechanical assembly critical to accuracy

As noted in the previous subsection, there are three significant measures of mechanical error due to the assembly of the IRISS. ε_x is the variation in the translational distance between $\hat{Y}$ and $\hat{Z}$ along $\hat{X}$ due to the circular arc being imperfectly mounted to its coupler with the rotational shaft. The other two errors, ε_y and ε_z, result from the surgical manipulator being mounted to the tool carriage. The alignment procedure for minimizing ε_x is illustrated in Figure 5. The coupling bracket and the arc are separated from the robotic platform and laid on a precision-ground surface. From the CAD model, the nominal dimensions x, ϕ and therefore h can be determined such that the axis of the circular arc, $\hat{Y}$, intersects the axis determined by the coupling bracket, $\hat{Z}$. If the arc is assumed to be perfectly circular, then by contacting a point x_0 with the ground, the arc can be rigidly secured to its mounting bracket by enforcing the distance h between the point x_h and the surface. This is realized by implementing a series of precision feeler gauges to maintain the distance h while the arc is physically secured to its bracket.

For the positional error ε_y, the components responsible for producing this error were machined and assembled according to best engineering practices. Because no capability exists for precision adjustment after mounting, these components were mounted and then measured to characterize the magnitude of error. For this process, the circular arc along with its mounted tool carriage and surgical manipulator were secured inside the workspace of a CNC mill. A Mitutoyo dial test indicator (12.7μm accuracy) was used to ensure that the rotational shaft and circular arc were parallel, and to zero the x and y positions of the mill about the calculated RCM position. In this way, the error in the y direction, corresponding to ε_y, was measured to be 0.058±0.025 mm
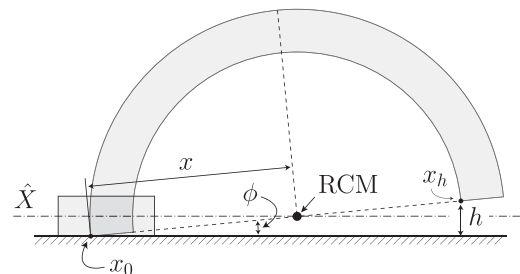

FIGURE 5　Schematic diagram of the procedure for aligning the circular arc with its mounting bracket

by repeating this measurement methodology until the offset error was lower than the combined accuracy of the tolerance stack-up.

4 | MECHATRONIC AND SOFTWARE DESIGN

The system architecture of the IRISS is shown in Figure 6. The IRISS is actuated by brushed DC servo motors, which are driven by current-type drive electronics. The position of each joint is measured by rotational optical encoders, with the manufacturer-reported resolutions shown in Table 1. Servo-level feedback control is based on the reference signals of the master manipulator and the encoder outputs of the joints. The data acquisition of the master manipulators and control for the IRISS are implemented on a National Instruments PXI real-time target with sampling rate of 1 kHz, as shown in Figure 7.

The IRISS has been designed such that it allows for 3D visualization using a standard stereoscopic ophthalmic microscope. Instead of being fed to an eyepiece, both optical channels of the microscope are directed to a TrueZoom 3D Surgical Camera (TrueVision Systems) that acquires video feeds of the surgical field. The video feeds are then used to provide a 3D visualization of the surgical scene to the surgeon. The video feeds are arranged in a standard side-by-side 3D format and then displayed using a 3D monitor with passive glasses.

Using the video feed, the surgeon can command the IRISS using the master surgical controller. During motion of surgical instruments, reference commands for joint angles are generated by the master surgical controller and modified with a selection of appropriate motion scaling such that the surgical precision can be increased. Tremor reduction is achieved by processing and filtering the frequency of motion through a simple moving average. In addition, the choice of which surgical instrument to engage as well as the irrigation and aspiration force commands for I/A tools are provided through a graphical user interface or through a standard foot pedal. High-level process monitoring of the system is also available to the surgeon including the ability to terminate the procedure. Less than 10 ms was measured for the communication latency from the master surgical controller to the slave controller, which is negligible compared to the reaction time of a typical human surgeon performing endoscopic surgery (approximately 360 ms) as shown by Zheng[27].

A finite state machine, as shown in Figure 8, is adopted as the software architecture for the IRISS control. After system initialization, all four mechanical joints are incremented through their range of motion until they trigger the photo-interrupter limit sensors. At this point, the joint values are recognized as the mechanical homed positions, and the robotic frame of reference is reset based on this repeatable initial configuration. The arm and the carriage of the robot are then moved to a predefined initial position. This homing procedure facilitates the accuracy and repeatability of the motion control.

Two lasers were mounted onto the tool carriage in such a way as to intersect at the RCM (see Section 5.1). Even though the RCM is ordinarily an invisible point in space, this setup allows for its visualization: when a surface blocks the path of the laser beams, the beams manifest
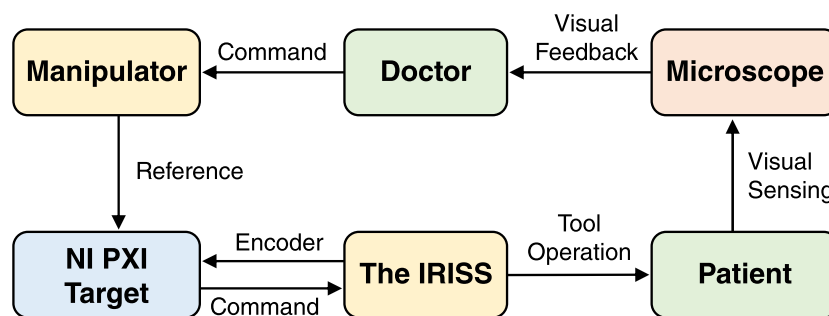

FIGURE 6 System architecture

TABLE 1 Resolution of optical joint encoders

Joint	Count/Rev.	Gear ratio	Resolution
θ_1	4000	100:1	0.90 mdeg/count
θ_2	2048	588:1	0.30 mdeg/count
d_3	1024	60:1	1.26 μm/count
θ_4	1024	17:1	20.7 mdeg/count

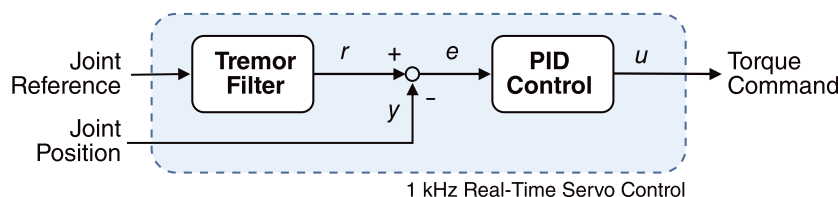**FIGURE 7** Real-time servo control loop conducted by standard PID controllers
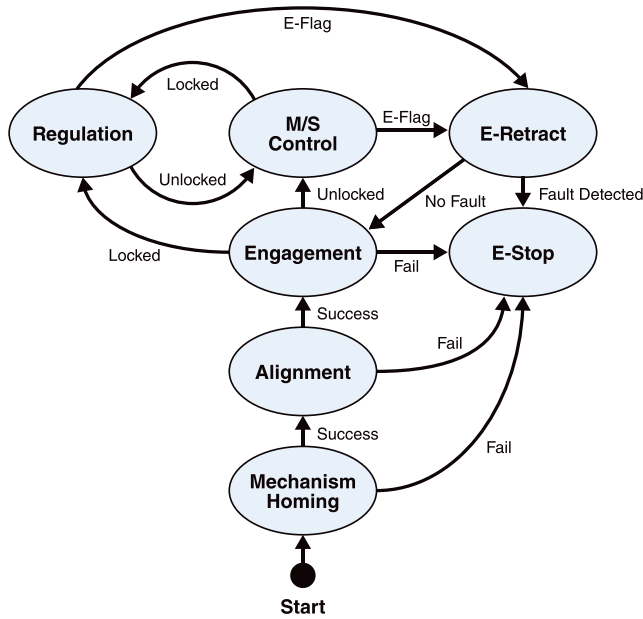
FIGURE 8 Finite state machine for control of the IRISS

FIGURE 9 CAD model of the RCM laser tool holder (isometric view)

5 | SYSTEM EVALUATION AND PERFORMANCE

5.1 | RCM laser design and calibration

themselves as visible points of light. Due to their prealigned configuration, when the separate points merge into one, the single visible point is known to be coincident with the RCM. In this way, aligning the mechanical RCM of the IRISS to the surgical incision point can be automatically performed by integrating control of the automated XYZ stage with computer-vision guidance. After the surgeon assigns the surgical incision point, visual feedback guides the stage to first align one of the laser spots to the incision point, and then registers the optical axis of the aligned laser. Alignment of the RCM to the incision point is achieved by moving the stage along the registered optical axis and searching for the minimal detected area of the laser points on the microscope image.

With the alignment procedure accomplished, the IRISS is ready for surgery, and the surgical instrument is moved to an initial configuration with the tool tip 3 mm away from the incision point (at $\hat{Y} = -3$ mm). At this point, the surgeon can control the IRISS with the master surgical manipulator. In addition, a lock function is provided to the surgeon to maintain the robot at a fixed position without the need to physically hold the master surgical controller. This function is used when the operation requires a temporary pause.

For experimental safety reasons, emergency shutdown of the IRISS is incorporated into the design of the finite state machine. If the homing procedure cannot be finished in a scheduled time period, the system will automatically shut down the actuators. The same feature is also realized when RCM alignment or the tool initialization fails. However, it is dangerous to shut down the robot during an operation in progress, especially when the instrument remains inside the eye. To prevent this problem, an emergency retraction of the instrument is performed immediately once an error flag is thrown; for example, when movement of the eyeball is detected. After retraction, the actuators will be shut down only if a fault is detected in the system. Otherwise, the system state will return to tool engagement and allow the surgeon to regain control of the tool. The system described above was implemented on a National Instruments PXI system running LabVIEW on a Real-Time Operating System.
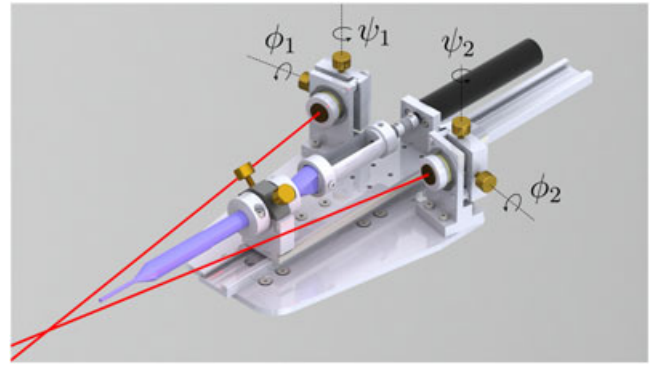
While each arm of the IRISS is specifically designed to have an RCM, a method is required to align each mechanical RCM point, $\boldsymbol{p}_{RCM}$, to the desired surgical incision points, $\boldsymbol{p}_I$, of the eyeball. Here, we consider only one RCM because the discussion applies identically to either. For this purpose, two stationary lasers were mounted onto the tool carriage, aligned in such a way as to intersect at $\boldsymbol{p}_{RCM}$ (Figure 9). Thus, when an eye is within the workspace of the manipulator, the laser beams will result in a single visible point on the corneal surface when $\boldsymbol{p}_{RCM} = \boldsymbol{p}_I$, and two distinct points when $\boldsymbol{p}_{RCM} \neq \boldsymbol{p}_I$.

Due to mechanical construction error of the lasers themselves, as well as the error in assembly and manufacturing tolerance stack-up of the laser mount subsystem, it cannot be guaranteed that the laser beams will accurately intersect at $\boldsymbol{p}_{RCM}$ after mounting. For example, typical commercial LED lasers have a deflection angle of $\pm 10°$ and a beam offset of ± 1 mm. This fact necessitates a mechanism for post-mounting precision adjustment on the laser mounts, which are incorporated into the design as two orthogonally mounted thumb screws. The laser is secured in a spherical bearing, and the thumb screws—when tightened—push into the laser housing, thereby changing the pitch angle ϕ_i and the yaw angle ψ_i of the laser beam. Compression springs provide a return motion.

The laser beams were independently aligned to pass through $\boldsymbol{p}_{RCM}$ by a manual, two-step procedure. First, a flat precision-ground plate was mounted perpendicular to the fixed robot base and placed such that its surface was aligned with the $\hat{Z}$ axis. The carriage was then repeatedly cycled through its θ_2 rotation and the laser yaw angle ψ_i manually adjusted until the rotational motion repeatedly produced a stationary laser point on the flat plate. Once satisfied, the angular deflection in ψ_i was considered to be sufficiently reduced. Second, the plate was moved along its normal direction (along $\hat{X}$) and the laser pitch angle ϕ_i was manually adjusted such that the laser point remained stationary as the plate was moved, thereby sufficiently reducing the angular deflection in ϕ_i. Once complete, the process was repeated on the other laser. After this alignment process, the lasers were considered to be aligned to intersect at the RCM and could be confirmed by actuating the tool tip through the RCM and noting the laser deflection. While the manual nature of this process was slow and inherently inaccurate, it need only be performed

once, and was considered adequate for the purpose of visualizing the RCM location in space and aligning the RCM with a surgical incision in the eye.

5.2 | RCM evaluation procedure

5.2.1 | RCM theory

The RCM of an ideal surgical manipulator is the point in space, p_{RCM}, through which the centreline of the surgical instrument is constrained to pass regardless of the pose in the workspace. However, due to errors in misalignment and assembly, this condition is never satisfied in practice for any robotic manipulator. Therefore, the definition of the RCM is revised as follows. Given n poses of a surgical instrument, the RCM is defined as

$$p_{RCM} := \arg\min_{p} J(d_1, \ldots, d_n) \qquad (7)$$

where d_i is the Euclidean distance from $p \in \mathbb{R}^3$ to the centreline of the surgical instrument in pose i and J is a cost function chosen from an appropriate physical meaning. This is shown schematically in Figure 10.

The purpose of a mechanically constrained RCM is to avoid stress in the corneal tissue at the incision point. For this reason, an appropriate choice for J is the maximum Euclidean distance from p to each pose centreline. This can be written in terms of the ∞-norm as

$$J_\infty(d_1, \ldots, d_n) := \|(\|d_1\|, \ldots, \|d_n\|)^\mathsf{T}\|_\infty \qquad (8)$$

$$= \max_i \|d_i\|. \qquad (9)$$

The minimization of equation (9) can be formulated as a second-order cone problem in which p_{RCM} minimizes $J_\infty(d_1, \ldots, d_n)$. Physically, p_{RCM} minimizes the maximum stress applied to the corneal tissue of the eye during surgical procedures.

Although the ∞-norm solution is physically meaningful, its computation is costly because it involves solving a convex program. The 2-norm is more convenient for its computational simplicity even though its physical meaning is not as apparent. For n poses, the cost function associated with the 2-norm is the sum of the squares of the Euclidean distance between p and each centreline

$$J_2(d_1, \ldots, d_n) := \|d_1\|^2 + \ldots + \|d_n\|^2. \qquad (10)$$

The 2-norm solution minimizes the variance of the sum of the squares of the normal Euclidean distance from the RCM to the centreline. While the physical meaning is not apparent, it is a useful metric of the performance of the RCM. For the purpose of evaluating the performance of the IRISS, both metrics were calculated and compared.

The overall approach to measure the location of the RCM and evaluate its 'performance' is outlined next. First, stereo cameras were calibrated and used to capture n pairs of images of n different instrument poses. The instrument location in each image was identified and used to determine the three-dimensional centreline pose by stereo triangulation. The cameras were considered to be simple projective (pinhole) cameras,[28] some radial distortion[29] was assumed, and the intrinsic and extrinsic calibration parameters were determined.[30,31]

To triangulate the centreline positions, the cameras must first take an image of the centreline. This is impossible to accomplish directly because the actual centreline is hidden inside the surgical instrument. However, the shafts of intraocular surgical instruments are typically cylindrical, regardless of the shape of the end effector. By using images of line sections that correspond to the edges of the cylinder image, it is possible to compute the image of the centreline. Through a related process to that described by Wilson[32], the centrelines can then be triangulated into 3D space.

5.2.2 | Localization of tool edges

To determine the three-dimensional tool centrelines, it is necessary to localize the tool edges in each image of all captured tool poses. To better represent the true performance of the IRISS, tool poses were captured over the entire range of the workspace of the manipulator. However, the range of possible motion results in a tool tip that can be located anywhere within a large cone-shaped volume (approximate height 100 mm, radius 70 mm), necessitating a wide angle of view to capture all possible poses. As a result, the small (1.63 mm diameter) tool tip used for this study is rendered approximately 3–5 pixels in width in the captured images. In addition, the I/A tool was chosen for this test because a specially designed substitute with favorable optical properties would not have been representational of actual surgical performance. However, the I/A tool is reflective and lacks strong visual contrast with its environment. For these reasons, a custom, sub-pixel localization algorithm was developed to determine the tool pose in the captured images, and is briefly described next.

The tool localization algorithm consists of three steps. First, the approximate location of the tip of the tool is located by applying the Features from Accelerated Segment Test algorithm,[33] which locates and ranks feature points, the strongest of which is assumed to be the approximate location of the instrument tip. Second, principal component analysis is performed on the region surrounding the approximate location of the instrument tip, where the first principal component (largest variance) describes the approximate orientation of the instrument. The direction of the instrument is established by a grayscale sampling method. Third, the Accurate Sub-pixel Edge Location method[34] is applied to the region surrounding the instrument and it returns edge point candidates with sub-pixel resolution. These points are categorized into 'top' edge points and 'bottom' edge points and fitted with a least-squares regression line. The final result of this algorithm is a pair of line segments that describe the two instrument edges in a single robotic manipulator pose. This process is then repeated on each of the captured images in the set.
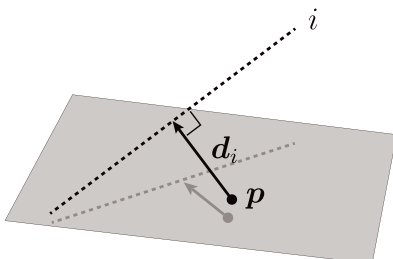

FIGURE 10 Schematic representation of the definition of the RCM

TABLE 2 Measured and calculated RCM-associated error

Error	Norm	Mean	RMS	Max.	Std.
e_{eval}	J_2	0.73	0.84	1.86	0.41
e_{eval}	J_∞	0.92	0.98	1.64	0.34
e_{img}	J_2	0.30	0.32	0.49	0.12
e_{img}	J_∞	0.34	0.36	0.55	0.13

All values are in units of mm.

5.2.3 | Measured error of the RCM

Having determined the edge line segments of the instrument in each image, the centrelines of the n instrument poses were calculated, and the RCM was computed, from the triangulation procedure described by Wilson[32]. 'Performance metrics' of the RCM were computed as statistical measures of the values of d_i (the Euclidean distance from the calculated p_{RCM} to the centreline of the surgical instrument for each instrument pose i). These results are reported in the first two rows of Table 2 as values of e_{eval} calculated with the cost functions J_∞ (equation 8) and J_2 (equation 10).

As expected, J_∞ minimizes the maximum distance from the centrelines to p_{RCM}, while J_2 minimizes the RMS of the distance from the centrelines to p_{RCM}. For p_{RCM} calculated with the ∞-norm, the maximum stress in the corneal tissue at the incision point is reduced; for p_{RCM} calculated with the 2-norm, the average stress in the corneal tissue over the manipulator's range of motion is reduced. Therefore, the choice of cost function depends on what is of more importance for a surgical procedure: reducing the magnitude of the largest stress experienced at the incision point or minimizing the average stress at the incision point over the duration of surgery.

5.2.4 | Error estimation of RCM evaluation procedure

The error in the RCM evaluation procedure described in Section 5.2.2 can be decomposed as

$$e_{eval} = e_{img} + e_{RCM} \tag{11}$$

where e_{eval} is the combined error in the RCM evaluation (measured and calculated from the previously described procedure), e_{img} is error introduced from the image-processing algorithm (subsection 5.2.2) and e_{RCM} is error introduced from mechanical sources of the IRISS. Because the primary concern was to evaluate the magnitude of mechanical errors e_{RCM}, it is necessary to know e_{img}.

The RCM evaluation procedure described in this section used two Logitech Carl Zeiss Tessar HD 1080p webcams with a resolution of 640×480 px. Intrinsic camera properties were computed with algorithms originally developed by Zhang[29] while extrinsic camera properties were computed using a rough estimate via the linear eight-point algorithm[35] followed by a nonlinear bundle adjustment. All calibration of camera parameters was implemented using functions from the MATLAB camera calibration toolbox.[36]

To characterize the resolution of the stereo camera setup as a sensor, a three-dimensional matrix of points with known geometry (a 5×7 checkerboard with square edge length of 5 mm) was measured at a distance within the workspace of the IRISS. Forty sets of two-image pairs were taken of the checkerboard in different orientations and positions, and a matrix of corner points was reconstructed from the images through triangulation. The Euclidean distances between these points were calculated and compared with the known edge length. The median camera reconstruction error was calculated to be 0.03±0.01 mm, where the uncertainty represents the standard error ($n = 1638$).

To test the magnitude of error caused by the image-processing algorithm, e_{img}, the algorithm was used to compute the centrelines of a benchmark device specifically designed to have a very precise RCM. The device developed for this analysis was a precision-ground, stainless steel, 1.63 mm shaft secured with a transition fit into a Heim HM3 all-steel, precision spherical joint. Because the spherical ball joint is sufficiently round, the RCM condition is enforced at the centre of the bearing with the centreline of the shaft intersecting the spherical centre. Therefore, any error in the RCM image-processing algorithm applied to the benchmark device can be attributed to errors introduced from the image acquisition and the image-processing algorithm and *not* from mechanical error.

Physically, the camera configuration and physical shaft dimensions of the benchmark setup were chosen to be analogous to the setup using the actual robot-mounted surgical tool. Therefore, any calculated error in the benchmark test was assumed to be representative of e_{img} during the robot-mounted surgical tool test. In short, the benchmark test provided a measure of e_{img}. The results are reported in Table 2 and suggest that the actual mean value of e_{RCM} must be less than 0.73 mm.

5.3 | Precision, accuracy, and mechanical performance

To judge the accuracy of the IRISS, the three-dimensional location of the surgical tool tip was measured using an optical coherence tomography

TABLE 3 Results of precision test

	RMS	SE	Max.	n
Point A	0.027	0.002	0.045	14
Point B	0.030	0.002	0.047	15

All values are in units of mm.

TABLE 4 Quantitative performance metrics of the IRISS joints

Metric	Value	Std.	Unit
θ_1 max. joint limit	+1.57	–	rad
θ_1 min. joint limit	−0.20	–	rad
θ_1 max. joint velocity	0.57	3.6×10^{-3}	rad/s
θ_2 max. joint limit	+0.70	–	rad
θ_2 min. joint limit	−0.70	–	rad
θ_2 max. joint velocity	1.10	0.0348	rad/s
d_3 max. joint limit	+25	–	mm
d_3 min. joint limit	−60	–	mm
d_3 max. joint velocity	131	2.95	mm/s
d_3 backlash	0.070	0.022	mm
d_3 stiction	4.2×10^{-3}	1.9×10^{-3}	mm
θ_4 max. joint limit	+0.52	–	rad
θ_4 min. joint limit	−0.52	–	rad
θ_4 max. joint velocity	44.9	0.23	rad/s

(OCT) system (ThorLabs Telesto-II V1 with LSM04 lens) and with the I/A tool mounted. The IRISS was commanded to move the tool to various points in its workspace, where the location of the tool tip was determined by the OCT and converted to physical units based on the known calibrated relationship. This analysis produces two sets of points: the location of the tool tip as calculated from the forward kinematics (the commanded position) and its location as measured by the OCT system. The difference between these points is a measure of the accuracy of the device and has a root mean square value of 0.205±0.003 mm, where the uncertainty represents the standard error ($n = 28$).

A similar procedure was used to judge the precision of the IRISS. The IRISS was commanded to move the tool tip to two points in its workspace, a distance of 0.345 mm apart, where the trajectory required actuation of all three joints. Thus, two groups of positions of the tool tip were obtained: OCT-measured tip positions when the tool was commanded to touch point A (at $\theta_1 = 15°$, $\theta_2 = 15°$ and $d_3 = -2.55$ mm) and OCT-measured tip positions when the tool was commanded to touch point B (at $\theta_1 = 5°$, $\theta_2 = -5°$ and $d_3 = -2.10$ mm). The centroid location of each group was determined and the distance between each location of the tool tip and this centroid was calculated. The relevant statistical measures are shown in Table 3 and provide a measure of the precision of the IRISS.

Finally, a series of quantitative performance metrics were measured to characterize the IRISS. Measured values are presented in Table 4. Backlash was measured as the difference between the initial and final positions of d_3 after the joint was commanded to move from a starting position to an intermediate position and back to its starting position. Stiction was measured as the average distance that d_3 'jumped' when the joint was commanded to move in its smallest possible increments (1.26 μm/count).

5.4 | Evaluation of surgical performance

Several surgical procedures required by cataract and retinal surgeries were tested in a clinical setting. The evaluation was performed on porcine eyes and the operating theatre is shown in Figure 11. For this experiment, a surgical microscope mounted with a stereo camera (TrueVision) was positioned over the eyeball as is typical with conventional interocular surgery. The surgeon was able to look at the display and see the same three-dimensional field of view as if viewing the surgical field directly through the microscope. By providing input motions through the master surgical controller, the IRISS was able to perform the following surgical procedures:

1. anterior lens capsulorhexis;
2. viscoelastic injection;
3. hydro-dissection;
4. lens aspiration;
5. retinal vein cannulation;
6. vitrectomy.

Of particular note, retinal vein cannulation—which requires a tool-positioning accuracy of 10 μm to access the vein—was performed to validate the ability of the IRISS to accurately execute precise tasks. Two surgical instruments were involved in this particular step: a light pipe to illuminate the posterior pole and a micro syringe for vessel cannulation. Thus, the unique ability of the IRISS to simultaneously manipulate two surgical instruments was demonstrated. Retinal vein cannulation was achieved by reducing the gain between input motions from the master surgical manipulator and reference commands sent to the slave manipulator. This allowed the surgeon to move the micro syringe into position and pierce the retinal vessel. Figure 12 (top) shows the micro syringe positioned adjacent to the retinal vessel just before cannulation. Figure 12 (bottom) shows the micro syringe in contact with the retinal vein during cannulation.

Although all of the completed tasks were considered clinically relevant procedures by the trained surgeons that performed them using the IRISS, retinal vein cannulation was specifically evaluated because it is a technically challenging and physically delicate operation. Furthermore, the IRISS is believed to be both the first robotic system to successfully create a round, curvilinear capsulorhexis essential for cataract surgery and the first to carry out an entire cataract extraction from beginning to end. Finally, the IRISS was assessed as possessing the required ranges of motion, dexterity and accuracy for delicate intraocular surgery. The details of the evaluation of the animal model are presented in full by Rahimy[25].
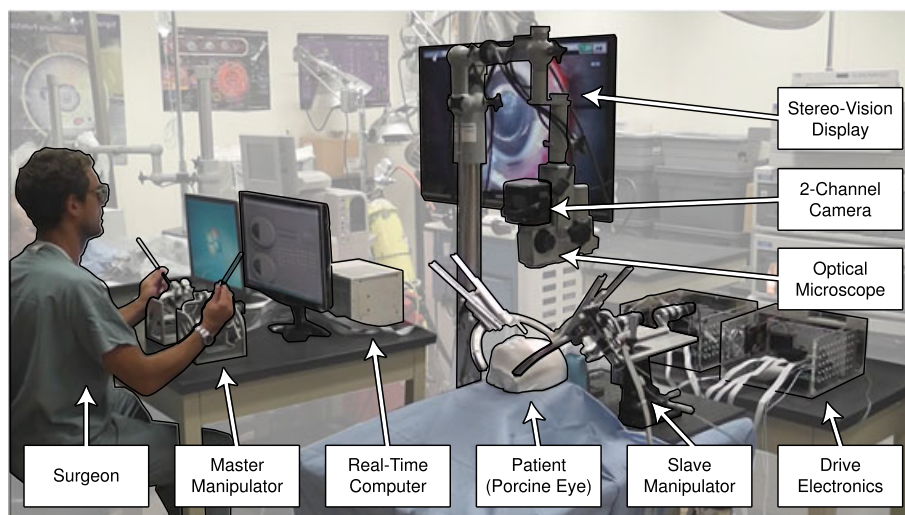

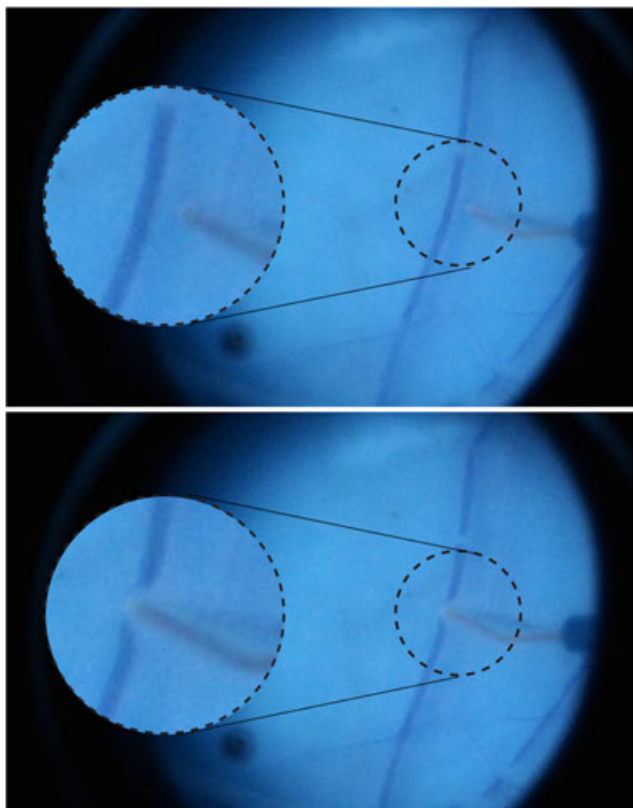**FIGURE 11** Experimental setup for surgical tests on porcine eyes

FIGURE 12 View of the surgical field through the microscope moments before retinal vein cannulation (top) and during retinal vein cannulation (bottom)

6 | CONCLUSION AND FUTURE WORK

This paper highlights the mechanical design and evaluation of an intraocular robotic interventional surgical system (IRISS). Developed as a necessary step towards fully automated intraocular surgery, the IRISS features the ability to simultaneously manipulate multiple surgical instruments with a large range of motion, mount any commonly used surgical instrument, change between tools using a simple tool-changing mechanism, and visualize and facilitate automated alignment of the RCM to the surgical incision using a set of lasers. The capabilities of the developed system were validated in a surgical theatre on post-mortem pig eyes and shown to be effective in completing many key steps in a variety of intraocular surgical procedures, as well as being capable of performing an entire cataract extraction from start to finish.

The IRISS was evaluated to possess a positional precision of the tool tip of 0.027±0.002 mm and accuracy of 0.205±0.003 mm, which is considered adequate for cataract removal and, through visual feedback, the more delicate retinal vein cannulation. The positional accuracy can be further improved by eliminating the error stack-up in assembly of the motor mounts, the arc–carriage interface and the instrument holder by fabricating these interfaces as single components. Also, fine-tuning mechanisms can be incorporated into error-prone points of contact to facilitate positional adjustments after assembly. The precision can be improved by reducing backlash, stiction, and the mechanical deformation in the motor gear train.

Future work includes fully automating cataract surgery by developing motion guidance and path planning of the IRISS through OCT

sensing and using visual servoing to compensate for eyeball movement. Furthermore, additional clinical experiments will be performed to validate the surgical performance of the IRISS. In addition to mechanical-based evaluation, clinical statistics such as success rate and completion time can provide insight into the future design directions of the intraocular surgical robotic system.

AUTHOR CONTRIBUTION

Wilson performed the mechanical design, fabrication and mechatronics, and developed the RCM evaluation method; Gerber performed the calibration, reassembly, mechatronics and evaluation of the RCM, precision and accuracy; Prince performed the mechanical design, fabrication and initial assembly and evaluations; Chen developed the laser alignment of the RCM and incision point, and performed mechatronics and evaluation of precision and accuracy; Schwartz contributed in asserting the surgical requirements and approving the conceptual design; Hubschman contributed in asserting the surgical requirements and approving the conceptual design, led evaluation of animal models and the clinical aspect of the development, and co-led the project team with Tsao; and Tsao conceived the IRISS, performed the conceptual design, led the engineering aspect of the development, and co-led the project team with Hubschman. The manuscript was first written by Wilson and Tsao and later rewritten by Gerber, Chen and Tsao with the addition of the evaluations of the laser alignment and enhancement of the mechanical precision and accuracy.

ACKNOWLEDGEMENTS

ORCID

Tsu-Chin Tsao iD http://orcid.org/0000-0003-2087-6221

REFERENCES

1. Buckingham RA, Buckingham RO. Robots in operating theatres. *BMJ.* 1995;311(7018):1479-1482.

2. Congdon NG, Friedman DS, Lietman T. Important causes of visual impairment in the world today. *JAMA.* 2003;290(15)(15):2057-2060.

3. Catalys precision laser system. http://www.optimedica.com/catalys-/overview, [Accessed: 2016-04-27].

4. Lensx laser. http://www.lensxlasers.com, [Accessed: 2016-04-27].

5. Palanker D, Schuele G, Friedman N, Andersen D, Culbertson W. Cataract surgery with oct-guided femtosecond laser. In: Optics in the Life Sciences, OSA Technical Digest (CD) (Optical Society of America), 2011: BTuC4, Monterey, CA, USA.

6. Son J, Bourges JL, Culjat MO, et al. Quantification of intraocular surgery motions with an electromagnetic tracking system. *Stud Health Technol Inform*. 2008;142:337-339.

7. Hubschman JP, Son J, Allen B, Schwartz SD, Bourges JL. Evaluation of the motion of surgical instruments during intraocular surgery. *Eye*. 2011;25(7):947-953.

8. Grace KW, Colgate JW, Glucksberg MR, Chun JH. A six degree of freedom micromanipulator for ophthalmic surgery. In: Proceedings of the IEEE International Conference on Robotics and Automation. Atlanta, GA, USA; 1993:630-635.

9. Merlet JP. Articulated device, for use in particular in robotics. Google Patents, 1991. US Patent 5,053,687.

10. Bourla DH, Hubschman JP, Culjat M, Tsirbas A, Gupta A, Schwartz SD. Feasibility study of intraocular robotic surgery with the da vinci surgical system. *Retina*. 2008;28(1):154-158.

11. Bourges JL, Hubschman JP, Wilson J, Prince S, Tsao TC, Schwartz S. Assessment of a hexapod surgical system for robotic micro-macro manipulations in ocular surgery. *Ophthalmic Res*. 2011;46(1):25-30.

12. Wei W, Goldman RE, Fine HF, Chang S, Simaan N. Performance evaluation for multi-arm manipulation of hollow suspended organs. *IEEE Trans Robot*. 2009;25(1):147-157.

13. Wei W, Goldman RE, Simaan N, Fine H, Chang S. Design and theoretical evaluation of micro-surgical manipulators for orbital manipulation and intraocular dexterity. In: Proceedings of the 2007 IEEE International Conference on Robotics and Automation. Roma, Italy; 2007:3389-3395.

14. Nasseri MA, Eder M, Eberts D, et al. Kinematics and dynamics analysis of a hybrid parallel-serial micromanipulator designed for biomedical applications. In: Proceedings of the 2013 IEEE/ASME International Conference on Advanced Intelligent Mechatronics (AIM). Wollongong, NSW, Australia; 2013:293-299.

15. Nasseri MA, Eder M, Nair S, et al. The introduction of a new robot for assistance in ophthalmic surgery. In: Proceedings of the 35th Annual International Conference of the IEEE Engineering in Medicine and Biology Society (EMBC). Osaka, Japan; 2013:5682-5685.

16. Nasseri MA, Gschirr P, Eder M, et al. Virtual fixture control of a hybrid parallel-serial robot for assisting ophthalmic surgery. In: Proceedings of the 5th IEEE RAS/EMBS International Conference on Biomedical Robotics and Biomechatronics. Sao Paulo, Brazil; 2014:732-738.

17. Barthel A, Trematerra D, Nasseri MA, et al. Haptic interface for robot-assisted ophthalmic surgery. In: Proceedings of the 37th Annual International Conference of the IEEE Engineering in Medicine and Biology Society (EMBC). Milan, Italy; 2015:4906-4909.

18. Ueta T, Yamaguchi Y, Shirakawa Y, et al. Robot-assisted vitreoretinal surgery: Development of a prototype and feasibility studies in an animal model. *Ophthalmology*. 2009;116(8):1538-1543.

19. Noda Y, Ida Y, Tanaka S, et al. Impact of robotic assistance on precision of vitreoretinal surgical procedures. *PloS One*. 2013;8(1):e54116.

20. Tanaka S, Harada K, Ida Y, et al. Quantitative assessment of manual and robotic microcannulation for eye surgery using new eye model. *Int J Med Robot Comput Assisted Surgery*. 2015;11(2):210-217.

21. Mitchell B, Koo J, Iordachita I, et al. Development and application of a new steady-hand manipulator for retinal surgery. In: Proceedings of the 2007 IEEE International Conference on Robotics and Automation. Roma, Italy; 2007:623-629.

22. He X, Roppenecker D, Gierlach D, et al. Toward clinically applicable steady-hand eye robot for vitreoretinal surgery. In: Proceedings of the ASME 2012 International Mechanical Engineering Congress and Exposition. Houston, Texas, USA; 2012:145-153.

23. He X, Roppenecker D, Gierlach D, et al. A master–slave robot for vitreo-retinal eye surgery. In: Proceedings of the 10th International Conference of European Society for Precision Engineering and Nanotechnology. Delft, Netherlands; 2010:3-6.

24. Smet de MD, Meenink HCM, Naus GJL, Oosterhout van EMW, Rosielle PCJN, Steinbuch M. Evaluation of a microrobotic surgical system for vitreoretinal surgery. In: Proceedings of the 12th EURETINA Congress. Milan, Italy; 2012.

25. Rahimy E, Wilson J, Tsao TC, Schwartz S, Hubschman JP. Robot-assisted intraocular surgery: development of the iriss and feasibility studies in an animal model. *Eye*. 2013;27(8):972-978.

26. Murray RM, Li Z, Sastry SS, Sastry SS. *A Mathematical Introduction to Robotic Manipulation*. Boca Raton, Florida, USA: CRC Press; 1994.

27. Zheng B, Janmohamed Z, MacKenzie CL. Reaction times and the decision-making process in endoscopic surgery. *Surg Endosc*. 2003;17(9):1475-1480.

28. Horn B. *Robot Vision*. Cambridge, MA, USA: MIT Press; 1986.

29. Zhang Z. Flexible camera calibration by viewing a plane from unknown orientations. *Proc 7th IEEE Int Conf Comput Vision*. 1999;1:666-673.

30. Ma Y, Soatto S, Kosecka J, Sastry SS. *An Invitation to 3-d Vision: From Images to Geometric Models*, Vol. 26. New York, NY, USA: Springer Science & Business Media; 2012.

31. Hartley R, Zisserman A. *Multiple View Geometry in Computer Vision*. Cambridge, England: Cambridge University Press; 2003.

32. Wilson JT, Tsao TC, Hubschman JP, Schwartz S. Evaluating remote centers of motion for minimally invasive surgical robots by computer vision. In: Proceedings of the IEEE/ASME International Conference on Advanced Intelligent Mechatronics (AIM). Montreal, QC, Canada; 2010:1413-1418.

33. Viswanathan DG. Features from accelerated segment test (fast). nd; 2009.

34. Trujillo-Pino A, Krissian K, Alemán-Flores M, Santana-Cedrés D. Accurate subpixel edge location based on partial area effect. *Image and Vision Comput*. 2013;31(1):72-90.

35. Longuet-Higgins HC. A computer algorithm for reconstructing a scene from two projections. Nature. 1981;293:133-135.

36. Bouget JY. Camera calibration toolbox for matlab. http://www.vision.caltech.edu/bouguetj, [Accessed: 2016-04-27].

SUPPORTING INFORMATION

Additional Supporting Information may be found online in the supporting information tab for this article.